fractal and fractional

MDPI

Article

Multi-Objective Load Frequency Optimization for Standalone Energy Supplies Using a Two-Tier FOPID Controller

Mohamed Nejlaoui and Abdullah Alghafis *

Department of Mechanical Engineering, College of Engineering, Qassim University, Buraidah 51452, Saudi Arabia; m.nejlaoui@qu.edu.sa
* Correspondence: a.alghafis@qu.edu.sa

Abstract

The global shift toward decentralized generation has established standalone energy supply systems as a vital solution for remote regions. However, the integration of intermittent renewable sources and the inherent lack of rotational inertia in power electronic interfaces create significant challenges for frequency stability. This study addresses these issues by introducing an original Two-Tier Fractional-Order PID (TTFOPID) controller designed for robust Load Frequency Control (LFC) in a hybrid system comprising solar, diesel, biodiesel, and battery energy storage (BESS). The research utilizes the Multi-Objective Imperialist Competitive Algorithm (MOICA), enhanced with an attractive and repulsive assimilation phase, to navigate the high-dimensional parameter space. A unique framework is established to simultaneously tune controller gains and high-level system parameters, specifically BESS sizing and droop settings. Results demonstrate that the MOICA-tuned TTFOPID provides superior performance, achieving a 72% improvement in the Integral of Time-Weighted Absolute Error (ITAE) compared to NSGA-II and a 56% improvement in the Integral of the Square of Control (ISC) compared to MOPSO. Furthermore, robustness analysis validates the controller's stability against significant parametric variations. The study concludes that the integrated TTFOPID-MOICA approach provides a superior pathway for stabilizing autonomous energy supply systems while protecting hardware longevity through optimized control effort.

Keywords: energy supply; fractional-order proportional–integral–derivative (FOPID); Optimization; multi-objective imperialist competitive algorithm (MOICA); control; renewable energy

Check for updates

Academic Editor: Norbert Herencsar

Received: 17 March 2026
Revised: 16 April 2026
Accepted: 18 April 2026
Published: 22 April 2026

Copyright: © 2026 by the authors. Licensee MDPI, Basel, Switzerland. This article is an open access article distributed under the terms and conditions of the Creative Commons Attribution (CC BY) license.

1. Introduction

The architecture of modern energy supply systems is undergoing a profound transition, driven by the global imperative to integrate renewable energy sources (RESs) and shift toward decentralized generation. Standalone energy supplies have emerged as a critical technical solution for ensuring consistent electricity in geographically isolated regions where extending a centralized grid is economically or technically unfeasible. These autonomous systems provide a vital lifeline for rural development and offshore infrastructure [1–3].

To guarantee reliability, a standalone energy supply typically functions as a hybrid entity, incorporating diverse technologies such as photovoltaic (PV) arrays, BESS, and conventional backup units like diesel or biodiesel generators [4–7]. While this configuration enhances energy independence, the intermittent nature of solar and wind generation

introduces intricate operational hurdles. Furthermore, the stability of these systems is frequently compromised by a lack of rotational inertia. The system is highly sensitive to sudden load changes, since renewable units are interfaced through power electronics rather than heavy rotating machinery [8,9]. These dynamics manifest as rapid frequency fluctuations that can lead to equipment damage or system-wide failure. Consequently, robust LFC mechanisms are fundamental to maintaining power quality [10,11].

Historically, the Proportional–Integral–Derivative (PID) controller has been the most prevalent tool for LFC due to its straightforward implementation. Various metaheuristic strategies, such as the Arctic Puffin Algorithm [12], Chaotic Optimization [13], and Cuckoo Search [14], have been proposed to refine these controllers. However, linear PID controllers often falter when faced with the severe nonlinearities of modern energy supplies [15,16]. To overcome these limitations, the engineering community has increasingly adopted Fractional-Order (FO) calculus. The FOPID controller introduces two additional parameters (the orders of integration and differentiation), allowing for much finer tuning of the system's frequency response [17,18].

Existing literature on FOPID parameter tuning is generally categorized into analytical and heuristic methodologies. Traditional analytical techniques include piecewise orthogonal function expansion, dead-time model rules, and methods centered on gain/phase margin specifications [19,20]. More recently, intelligent evolutionary algorithms, such as Particle Swarm Optimization (PSO) and Genetic Algorithms (GA), have been widely adopted to navigate the complex, high-dimensional parameter space of fractional-order controllers [21,22].

Beyond established methods, recent studies have introduced novel bio-inspired algorithms such as the Arctic Puffin Algorithm [23] and the Nutcracker Optimizer for fine-tuning LFC parameters in multi-area systems [24]. Furthermore, recent work by Almutairi et al. [25] has demonstrated the efficacy of a two-stage PID + Fuzzy controller for hybrid systems, emphasizing the trend toward multi-stage architectures to handle high renewable penetration. Similarly, comparative studies [26] underscored the importance of integrating Battery Energy Storage Systems (BESS) as primary frequency stabilizers in isolated grids.

While recent studies, such as [23], have proposed cascaded FOPID controllers for stability, they typically rely on traditional secondary control loops that lack the depth to handle simultaneous multi-source fluctuations. The Two-Tier FOPID (TTFOPID) proposed here differs structurally by implementing a two-stage compensation logic that specifically targets the decoupling of renewable-induced transients from load-induced deviations. By utilizing the first tier as a predictive filter for derivative action and the second tier for integral accumulation, the TTFOPID reduces sensitivity to fractional-order derivative noise (a nuance not addressed in standard cascaded models) thereby providing a smoother control signal under the high-frequency volatility of solar PV inputs.

Despite these advancements, a significant portion of current research remains focused on single-objective strategies [23–29]. In practice, however, control systems must navigate a landscape of conflicting performance indicators, requiring a deliberate trade-off between objectives. To address this, the present study utilizes the MOICA, specifically a variant enhanced with an attractive and repulsive assimilation phase [30,31]. This advanced optimizer is strategically employed to resolve the tension between rapid set-point tracking and system robustness by utilizing two competing performance indices: ITAE and ISC. Furthermore, although these recent advancements have improved frequency regulation, most contemporary research still treats controller tuning and the physical sizing of energy storage as independent problems [32–35]. For instance, recent optimization frameworks for energy supply system planning often focus on economic dispatch without simultaneously

optimizing the transient control gains required for stability. This study bridges that gap by proposing an integrated multi-objective approach that optimizes both the TTFOPID gains and the physical BESS scaling parameters. A summary of related work is presented in Table 1 to clearly distinguish the original contributions of this study from existing state-of-the-art methods.

Table 1. Comparative Synthesis of Related Work and Proposed Methodology.

Reference	Controller	Tuned Variables	Optimization Type	Disturbances	Reported Metrics
Ref [14]	PID	3	Single objective	Step Load	Absolute integral error (IAE)
Ref [15]	PID	3	Single objective	Step Load	Absolute integral error (IAE)
Ref [17]	FOPID	5	Multi-objective	Step Load	ISE and ITSE
Ref [22]	FOPID	5	Single objective	Step Load	ITAE
Ref [23]	Cascade FOPID	5	Single objective	Solar irradiance	ITAE
Ref [24]	PID	3	Multi-objective	Solar irradiance	Cost and pollutant emission
Ref [25]	PID + Fuzzy	9	Single Objective	Hybrid Renewables	ITAE
Ref [27]	FOPID	5	Single Objective	Step Load	Rotor speed deviation
Ref [33]	PID	3	Single Objective	Step Load	ITAE
Ref [35]	PID	3	Single Objective	Solar irradiance	ITAE
Proposed	Two-Tier FOPID	12	Multi-Objective	Step Load and Solar Fluctuations	ITAE and ISC

The significant contributions of this research are as follows:

- Development of a fully fractional TTFOPID controller, providing a higher degree of freedom for precise frequency regulation and effective decoupling of fast/slow dynamics.
- Application of the enhanced MOICA method to handle the complex, high-dimensional search space required for cascaded fractional architectures.
- Establishment an optimization framework that links low-level controller tuning with high-level system design (BESS sizing and droop settings).
- Comprehensive simulation-based validation, demonstrating that the MOICA-tuned TTFOPID consistently outperforms conventional PID, FOPID, and other state-of-the-art methods.

The remainder of this paper is organized as follows: Section 2 describes the mathematical modeling of the system; Sections 3 and 4 detail the optimization methodology and the MOICA; Sections 5 and 6 analyze the simulation results and robustness; and Section 7 concludes the work.

2. Energy Supply Modelling

The architectural configuration of the evaluated energy supply system, as detailed in Figure 1, represents a hybrid model designed for LFC analysis.

This integrated energy supply incorporates a diverse suite of generation assets, featuring photovoltaic (PV) arrays for renewable production, alongside diesel and biodiesel-driven generators and a BESS to ensure a consistent power balance for localized load demands. While the system is engineered for autonomous operation, it is designed with the capability to interface with a primary utility grid. However, for the scope of this study, the system is operated in a standalone (islanded) configuration by keeping the main circuit breaker at the Point of Common Coupling (PCC) open. This allows for a rigorous evaluation of the TTFOPID controller under the high-volatility conditions inherent to isolated energy supplies. The coordination of this multi-source environment is managed by a centralized control center. Within the schematic, the structural hierarchy is clearly delineated by color-coded flow paths: the red lines represent the cyber-layer of data communication links for feedback and control synchronization, while the blue lines illustrate the physi-

cal power flow paths that facilitate the transmission of electrical energy across the entire supply system.

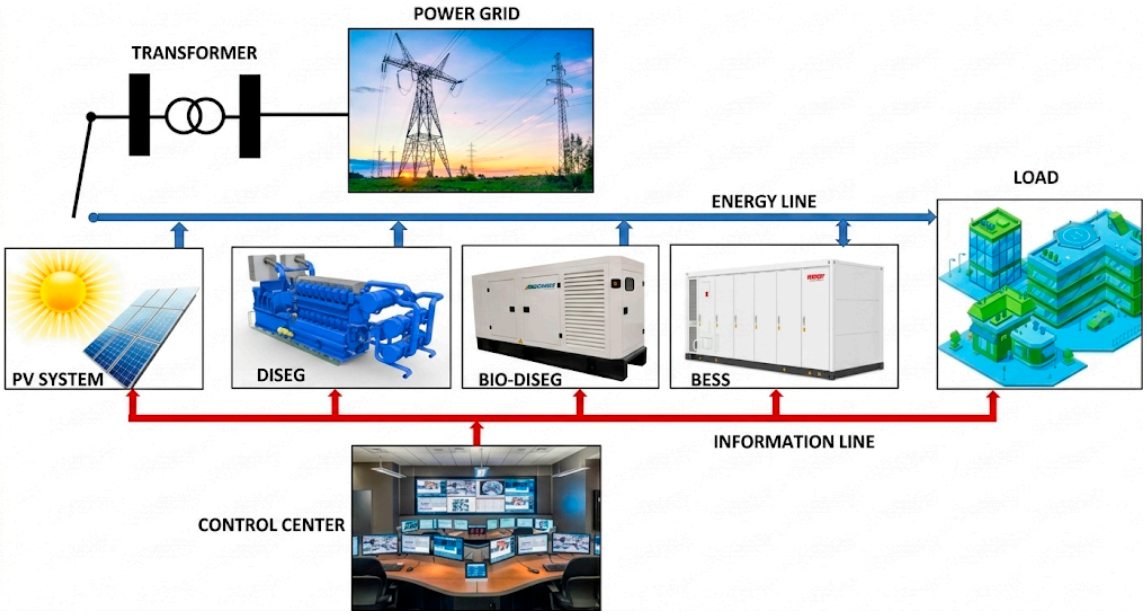


Figure 1. Energy Supply System structure.

2.1. Photovoltaic (PV) System

The PV assembly is composed of solar arrays, DC-to-AC inverters, and the necessary hardware for grid integration, which work in unison to transform solar radiation into electrical power. The operational efficiency of this system is highly sensitive to external environmental factors, particularly ambient irradiance and the thermal state of the module surfaces. Mathematically, the electrical generation of the PV unit is characterized by the interaction between the available solar flux, the module's surface temperature, the total area of the panels, and the overall conversion efficiency. This dynamic is formalized as [32]

$$P_{pv} = I.A.\delta.[1 - 0.005(T_s + 25)] \quad (1)$$

where δ the overall conversion efficiency of the system, A is the total effective surface area of the solar panel, I is the available solar flux and T_s represents the surface temperature of the PV modules.

To capture the system's transient characteristics, a first-order transfer function model is utilized [32]. In this framework, the PV system's behavior is defined by a proportional gain, K_{pv}, and a specific time constant, T_{pv}. The following equation provides the mathematical representation of this dynamic response [23]:

$$G_{pv}(s) = \frac{K_{pv}}{1 + sT_{pv}} \quad (2)$$

This simplified model is highly effective for LFC studies as it represents the inherent delay in power electronics and inverter switching without requiring the complexity of a full circuit simulation.

2.2. Diesel Engine Generator (DISEG)

The Diesel Engine Generator (DISEG) unit is a fundamental component for preserving frequency stability within modern power systems, especially in autonomous energy supply and hybrid generation configurations. This assembly comprises a diesel engine, a governor,

and a turbine; the engine transforms the chemical energy stored in fuel into mechanical torque, which is subsequently converted into electrical power.

The transient performance of the DISEG unit is largely defined by the governor time constant (T_g) and the engine–turbine time constant (T_t) [33]. These variables represent the inherent mechanical delays and response times of the hardware during the frequency adjustment process. As shown in Equation (3), the transfer function model of the DISEG within the proposed LFC framework is characterized as the mathematical product of two first-order lag elements [33]:

$$G_{DISEG}(s) = \frac{1}{1+sT_g} \cdot \frac{1}{1+sT_t} \tag{3}$$

2.3. Bio-Diesel Engine Generator (BIO-DISEG)

Functioning in a manner analogous to a standard diesel unit, the BIO-DISEG system is distinguished by its use of biodiesel sourced from renewable biological matter. This substitution offers a sustainable advantage by lowering carbon footprints and mitigating greenhouse gas emissions within the energy supply. From a mechanical standpoint, the unit comprises a biodiesel-powered internal combustion engine, a speed regulation governor, and a turbine. While its architecture mirrors traditional systems, the unique chemical properties and combustion profile of biodiesel result in distinct transient behaviors compared to fossil-fuel counterparts [27]. In the context of the LFC framework, the BIO-DISEG dynamics are mathematically modeled through a series of first-order transfer functions. These functions represent the governor and the engine–turbine responses, defined by the time constants T_{va} and T_{be}, respectively. The integrated frequency response of the unit during load variations is formalized in Equation (4), which serves as a critical component of the overall system stability analysis [33].

$$G_{BIO\text{-}DISEG}(s) = \frac{1}{1+sT_{va}} \cdot \frac{1}{1+sT_{be}} \tag{4}$$

2.4. BESS System and SOC-Managed Droop Control

In an autonomous energy supply system where renewable sources serve as the primary generation units, the integration of a BESS is vital for maintaining system integrity. By utilizing a droop control mechanism regulated by the State of Charge (SOC), the BESS efficiently counters power imbalances and provides high-precision frequency stabilization [34].

2.4.1. Modeling of BESS State of Charge (SOC) Dynamics

The SOC of a battery unit is determined by the time-integral of the power flow. Under the assumption of a stable battery voltage, the instantaneous SOC is calculated as [34]:

$$SOC(t) = SOC_0 + \frac{1}{E \times h}\int_0^t P_{BESS}(t)dt \tag{5}$$

In the Laplace domain, the transfer function representing the relationship between the power deviation (ΔP_{BESS}) and SOC dynamics is expressed as [34]:

$$\frac{\Delta SOC(s)}{\Delta P_{BESS}(s)} = \frac{1}{E \times h} \times \frac{1}{s} = \frac{1}{K_E\, s} \tag{6}$$

where SOC_0 is the initial state, E denotes the battery capacity (MWh), and h is the conversion factor (3600 s/h). K_E serves as the lumped energy constant for the BESS.

2.4.2. Enhanced Droop Control with SOC-Based Feedback

Under a standard droop framework, the BESS modifies its power output in direct response to frequency shifts (Δf). To prolong battery lifespan and ensure operational safety, an SOC-dependent frequency offset (f_{offset}) is introduced. The refined droop control law is defined as [35]:

$$\Delta P_{BESS}(t) = \frac{1}{R_{BESS}} \times [\Delta f(t) - f_{offset}(t)] \quad (7)$$

The frequency offset is characterized by the feedback loop $f_{offset}(t) = \Delta SOC(t) \times K_f$ where the gain K_f is determined by the maximum allowable frequency deviation and the total SOC range. This mechanism ensures that the droop response is dynamically adjusted based on current energy levels, preventing hazardous overcharging or deep discharge cycles. Integrating this with the SOC dynamics yields the overall transfer function [35]:

$$\frac{\Delta SOC(s)}{\Delta f(s)} = \frac{1}{R_{BESS}} \times \frac{1}{E \times h} \times \frac{1}{s} = \frac{1}{R_{BESS}\, K_E\, s} \quad (8)$$

2.4.3. Parallel Coordination and Parameter Scaling

To optimize stability in larger energy supply systems, multiple BESS units are operated in a parallel configuration. In this setup, the aggregate droop resistance is decreased by a factor of Y (representing the number of units), while the total energy capacity is scaled by a factor of X. Consequently, the combined BESS model is represented by an effective droop resistance of R_{BESS}/Y and an energy capacity of X·K_E. [35]

The parameters X and Y are not chosen arbitrarily; they are refined during the design phase using the MOICA. This co-optimization strategy ensures that the collective BESS behavior is fully synchronized with the TTFOPID, enabling efficient power sharing and reliable coordination under volatile load conditions, illustrated in Figure 2.

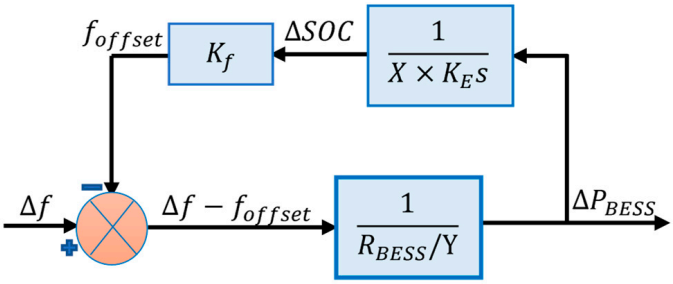


Figure 2. SOC-Compensated Parallel BESS Control Architecture.

To ensure operational safety and battery longevity, the BESS is restricted to a State-of-Charge (SOC) window of 20% to 80%. Within this framework, the SOC-managed droop mechanism dynamically throttles power injection or absorption as these physical limits are approached, effectively preventing hazardous overcharging or deep discharge cycles.

2.5. Structure of the TTFOPID Controller

This research presents an original two-tier Fractional-Order PID (FOPID) controller, designed to refine LFC in autonomous energy supply systems. The framework is specifically developed to navigate the complexities introduced by high photovoltaic (PV) penetration and volatile load demands. Moving beyond traditional PID methods, this design utilizes TTFOPID loops, providing enhanced precision, flexibility, and robustness. The operational parameters of this controller are fine-tuned using the MOICA method.

The proposed two-tier architecture features a dual-layer configuration designed for superior dynamic regulation. The primary outer loop manages the Area Control Error (ACE) to dampen broad deviations, while the secondary inner loop refines the response through high-speed fractional-order adjustments (see Figure 3).

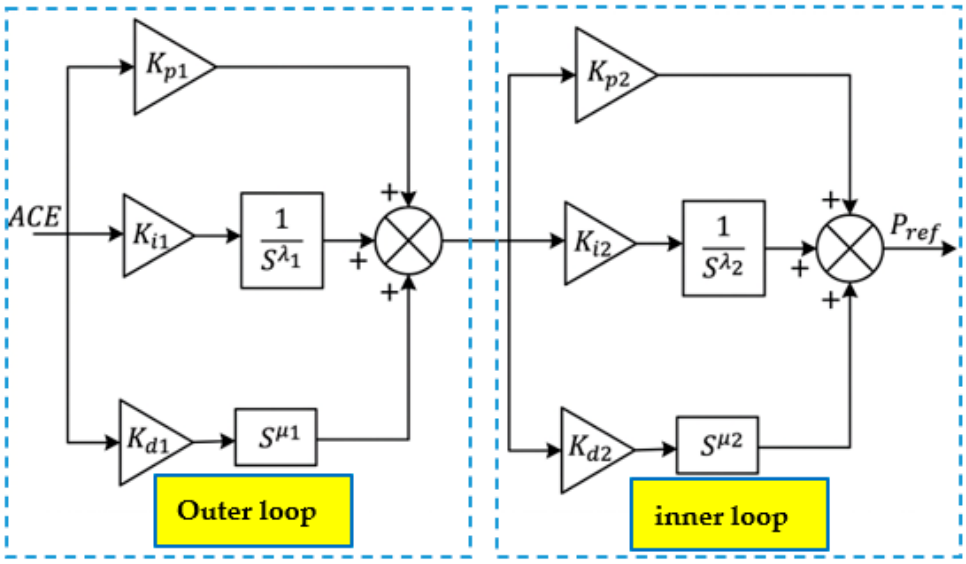


Figure 3. TTFOPID controller framework.

Unlike standard single-loop FOPID designs that limit fractional dynamics to one stage, this dual-layer approach implements fractional calculus across both segments. This integrated structure significantly bolsters the system's resistance to nonlinearities and uncertainties common in standalone energy supplies, a contribution that distinguishes this work from the existing LFC literature.

The transfer function for the i^{th} FOPID unit within the cascade is defined as [17]:

$$C(S) = K_{pi} + \frac{K_{Ii}}{S^{\lambda i}} + K_{di}S^{\mu i} \tag{9}$$

In this expression, i = 1,2 represents the outer and inner controllers, respectively. The terms K_{pi}, K_{Ii}, and K_{di} denote the proportional, integral, and derivative gains. The exponents λi and μi signify the orders of fractional integration and differentiation.

The finalized mathematical expression for the proposed control effort is:

$$P_{ref} = ACE \times \left(K_{p1} + \frac{K_{I1}}{S^{\lambda 1}} + K_{d1}S^{\mu 1}\right) \times \left(K_{p2} + \frac{K_{I2}}{S^{\lambda 2}} + K_{d2}S^{\mu 2}\right) \tag{10}$$

The reference power P_{ref} is defined in per-unit (p.u.) and represents the commanded change in power output required to balance the load.

The 'Two-Tier' designation distinguishes this controller from the 'Cascade Dual FOPID' found in the literature [23]. In this architecture, the first-tier functions as a high-frequency compensator, isolating the derivative component from the integral action managed in the second tier. This sequential filtering arrangement ensures that the derivative-induced chattering (prevalent in the single-loop cascaded structures of [23]) is suppressed before the control signal is processed for long-term error elimination. Consequently, the TTFOPID achieves a more robust equilibrium between fast transient response and steady-state accuracy in standalone environments.

The proposed control law follows a multiplicative Two-Tier architecture rather than a standard additive or nested loop. This selection is strategically motivated by the frequency-domain requirements of standalone hybrid systems. While additive control (e.g., parallel PID) provides linear corrective actions, the multiplicative cascade allows the second tier to function as a dynamic weighting filter. This configuration effectively decouples the low-frequency tracking (handled by the fractional integrator $S^{-\lambda i}$) from the high-frequency noise attenuation. Furthermore, unlike nested control which necessitates multiple feedback sensors for internal states, the TTFOPID achieves high-order compensation using only the frequency deviation error, thereby increasing the system's reliability and reducing computational overhead during real-time implementation.

The TTFOPID architecture provides several theoretical benefits that exceed the capabilities of classical integer-order cascade PID controllers. Specifically, the introduction of non-integer orders λi and μi allows for a non-integer slope in the Bode magnitude plot, enabling the controller to satisfy more complex frequency-domain specifications. Unlike the classical PID, which offers a fixed 90° phase lead/lag per operator, the fractional operators in the TTFOPID allow for a customizable phase lead/lag. This flexibility is critical for compensating for the diverse time constants of the diesel generators and the fast-acting BESS units simultaneously. Furthermore, the TTFOPID demonstrates an inherent iso-damping property, meaning the system's robustness is less sensitive to parametric uncertainties and gain fluctuations compared to its integer-order counterparts.

The stability of the standalone microgrid under TTFOPID control is analyzed using the state-space representation of the fractional-order system. Let the linearized closed-loop system be represented by the commensurate state-space form [36]:

$$D^q \boldsymbol{x}(\boldsymbol{t}) = \boldsymbol{A}\boldsymbol{x}(\boldsymbol{t}) + \boldsymbol{B}\boldsymbol{u}(\boldsymbol{t}) \tag{11}$$

where $\boldsymbol{A}$ is the state matrix of the closed-loop system, $\boldsymbol{x}(\boldsymbol{t})$ is the state vector, and q is the fractional order. According to Matignon's theorem, the system is asymptotically stable if and only if all eigenvalues (eig_i) of the state matrix $\boldsymbol{A}$ satisfy [36]:

$$\left|\arg(eig_i(\boldsymbol{A})) > q\frac{\pi}{2}\right| \tag{12}$$

This condition ensures that all poles of the fractional-order transfer function lie in the stable region of the Riemann surface. In this study, the TTFOPID parameters (λi and μi) are optimized to keep the eigenvalues of **A** deep within this stable zone, providing high damping for frequency oscillations.

2.6. System Modeling and Configuration of the Energy Supply System

The comprehensive LFC architecture for the autonomous energy supply system under study is illustrated in Figure 4. This model is intentionally streamlined to focus on critical power system elements, including diesel and biodiesel generators, a photovoltaic (PV) unit, and an SOC-managed BESS.

The framework replicates the complex transients typical of practical standalone systems, such as renewable output fluctuations, mechanical generator lag, sudden load shifts, and energy storage dynamics. This approach creates a robust yet computationally efficient environment for evaluating the proposed control strategy. Central to this architecture is the optimized TTFOPID controller, which processes frequency error signals to execute precise compensatory actions and maintain system equilibrium.

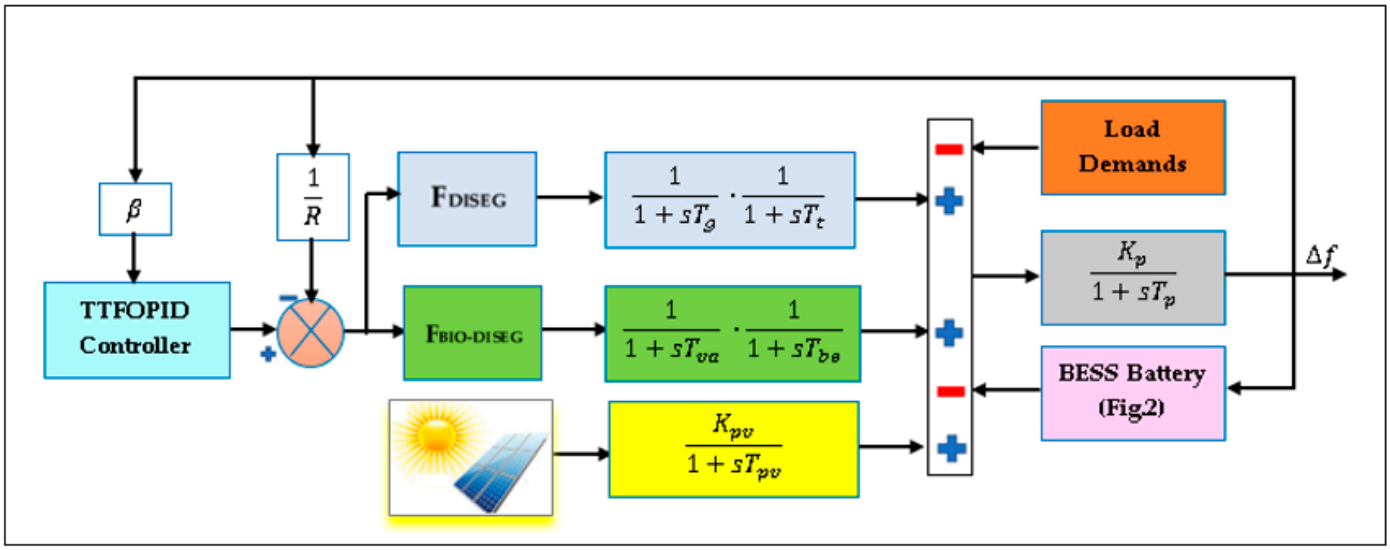


Figure 4. Block diagram of the energy supply model.

The transfer function models and parameters adopted in this architecture, as detailed in Table 2, are derived from established literature where they have been extensively validated against experimental data from practical microgrid installations. This ensures that the simulation environment accurately reflects the physical dynamics of real-world hardware, including mechanical lags and storage transients.

Table 2. Simulation parameters for the proposed energy supply system [23,27].

Parameters	Value	Parameters	Value	Parameters	Value
T_{PV}, K_{PV}	1.8 s, 1	Tg, Tt	0.1 s, 0.3 s	K_f	0.1/60
T_{va}, K_{va}	0.05 s, 1	Tp, Kp	10 s, 1	K_E	1.8
T_{be}, K_{be}	0.05 s, 0.002	β, R	0.2, 2.4	R_{BESS}	0.2

The control effort from the optimized TTFOPID unit is integrated with the frequency bias factor (β) and the regulation droop (1/R) to generate a reference power command. This aggregate signal is distributed among the diesel engine, biodiesel generator, and PV assembly. The combined power output is then balanced against real-time load demand to determine the system frequency deviation (Δf), which is fed back to the controller.

The transient behavior of the integrated generation units is characterized by a first-order transfer function, defined as [23]:

$$G_{ESS}(s) = \frac{K_p}{1 + sT_p} \tag{13}$$

In this representation, Kp signifies the steady-state gain, while Tp denotes the system time constant. This modeling approach effectively accounts for the collective damping and inertial properties of the primary power sources. Table 2 summarizes the numerical parameters for the energy supply system model.

In the proposed energy supply system, power sharing between the diesel and biodiesel generators is governed by their respective participation factors, F_{DISEG} and $F_{BIO\text{-}DISEG}$. While biodiesel supports sustainability goals through lower emissions, it is often constrained by higher operational costs and limited feedstock availability. Conversely, conventional diesel remains highly accessible and cost-effective despite its larger environmental footprint. To achieve a balanced trade-off between economic efficiency and environmental impact, this study implements an equal power-sharing distribution of 0.5 [23,27].

To achieve peak performance, an optimization framework is required to establish an objective function that balances control efficiency with the dynamic accuracy of the energy supply. This paper utilizes a multi-objective optimization approach to ensure the delivery of a highly robust LFC strategy.

3. Multi-Objective Performance Criteria and Constraint Definition

To achieve an optimal balance between rapid frequency recovery and control signal smoothness, the optimization process is governed by a multi-objective framework. This section outlines the mathematical indices used to quantify performance and the operational constraints that ensure the physical feasibility of the energy supply system.

3.1. Objective Function Formulation

The primary goal of the LFC is to minimize frequency excursions following a disturbance. For this purpose, the ITAE is employed as the first objective. The ITAE index is specifically advantageous for its time-weighting property, which heavily penalizes long-duration oscillations and facilitates a superior settling time:

$$ITAE = \int_0^{tsim} |\Delta f| \cdot t \cdot dt \tag{14}$$

where t represents the instantaneous simulation time and tsim denotes the total observation period.

However, relying solely on ITAE can lead to aggressive control actions that may saturate actuators or cause mechanical stress on the generators. To mitigate this, a second objective, the Integral Square of Control signals (ISC), is integrated into the optimization framework. This criterion penalizes excessive or high-frequency control efforts from the regulated sources, promoting system longevity and stability:

$$ISC = \int_0^{tsim} P_{ref}^2 \cdot dt \tag{15}$$

The ISC metric is computed as the integral of the squared sum of individual actuator signals (diesel governor and BESS power electronic interface). By penalizing the sum of these efforts, the optimizer avoids solutions that require aggressive, high-frequency switching of the actuators, thereby protecting mechanical components and power electronic switches from premature wear. Furthermore, the ISC metric serves as a critical surrogate for an economic cost model. In fact, by penalizing excessive and high-frequency control actions, the optimization inherently reduces thermal stress and chemical degradation on the BESS. Consequently, extending the operational lifespan and reducing long-term replacement costs.

By minimizing both ITAE and ISC simultaneously, the MOICA identifies a Pareto-optimal solution that ensures precise frequency regulation without compromising the operational integrity of the diesel/biodiesel units or the BESS.

3.2. Parameter Constraints and Search Space

To guarantee a robust and dependable optimization process, the search space for the TT- FOPID controller parameters is strictly bounded. These constraints prevent the selection of gains that could induce instability or non-causal behavior. The proportional (K_{pi}) and integral (K_{Ii}) gains are restricted to the range [0.1, 3], while the derivative gain (K_{di}) is limited to [0.1, 1]. To leverage the benefits of fractional calculus while maintaining a high phase margin, the fractional orders (λi and μi) are constrained between 0.5 and 1 [23–25].

Beyond the controller gains, the optimization process incorporates two discrete decision variables, X and Y. These variables dictate the BESS capacity configuration and its parallel power scaling, respectively. The scaling factors X and Y represent the number of parallel-connected BESS modules, where each base module has a rated energy capacity E_{base} (MWh) and power rating P_{base} (MW). The total capacity is thus $E_{total} = (X + Y).\ E_{base}$. In the optimization, X and Y are treated as integers in the range [0, 10]. While a value of zero is numerically possible, the search space is constrained to ensure at least one tier is active ($X + Y \geq 1$) to maintain the BESS contribution to frequency stability. This ensures that the resulting BESS dimensions are not only technically effective for frequency support but also economically feasible within the standalone energy supply context.

To ensure the practical feasibility of the proposed design, integer constraints are strictly imposed on the BESS decision variables X and Y. This is justified by the modular nature of commercial energy storage hardware, which is deployed in discrete units or racks; therefore, a continuous variable formulation would yield non-physical specifications that cannot be implemented in a real-world standalone energy system [23,27].

The stability condition $\left|\arg(eig_i(\boldsymbol{A})) > q\frac{\pi}{2}\right|$ was integrated into the optimization problem to ensure all Pareto-optimal solutions are inherently stable.

During the optimization process, any candidate "country" (set of controller parameters) that violates this stability constraint is assigned a high penalty value. This ensures that the final optimal solutions in the resulting Pareto front consist exclusively of stable and robust controller configurations.

In summary, the multi-objective optimization problem for the proposed energy supply system is formulated to simultaneously minimize the error criteria and control effort. The mathematical structure of the problem is defined as follows:

$$\begin{cases} Minimize\ ITAE = \int_0^{tsim} |\Delta f| \cdot t \cdot dt \\ Minimize\ ISC = \int_0^{tsim} P_{ref}^2 \cdot dt \end{cases} \tag{16}$$

Subject to the following parametric constraints:

$$\begin{cases} Controller\ Gains \begin{cases} 0.1 \leq K_{pi}, K_{Ii} \leq 3 \\ 0.1 \leq K_{di} \leq 1 \end{cases} \\ Fractional\ Oredrs : 0.5 \leq \lambda i, \mu i \leq 1 \\ State\ of\ Charge\ limits : 20\% \leq SOC \leq 80\% \\ BESS\ Configuration\ Variables : X, Y \in \mathbb{Z} \cap [0, 10]\ and\ X + Y \geq 1 \\ Stability\ Condition : \left|\arg(eig_i(\boldsymbol{A})) > q\frac{\pi}{2}\right| \end{cases} \tag{17}$$

To solve the optimization problem defined by Equations (16) and (17), the MOICA will be utilized.

4. Multi-Objective Imperialist Competitive Algorithm (MOICA)

The MOICA is a modern evolutionary optimization technique [30,37,38]. It is built upon the foundational principles of the original Imperialist Competitive Algorithm (ICA) but is adapted to manage multiple conflicting objectives simultaneously. The procedural flow of the algorithm is visually represented in Figure 5, with the specific operational phases detailed below.

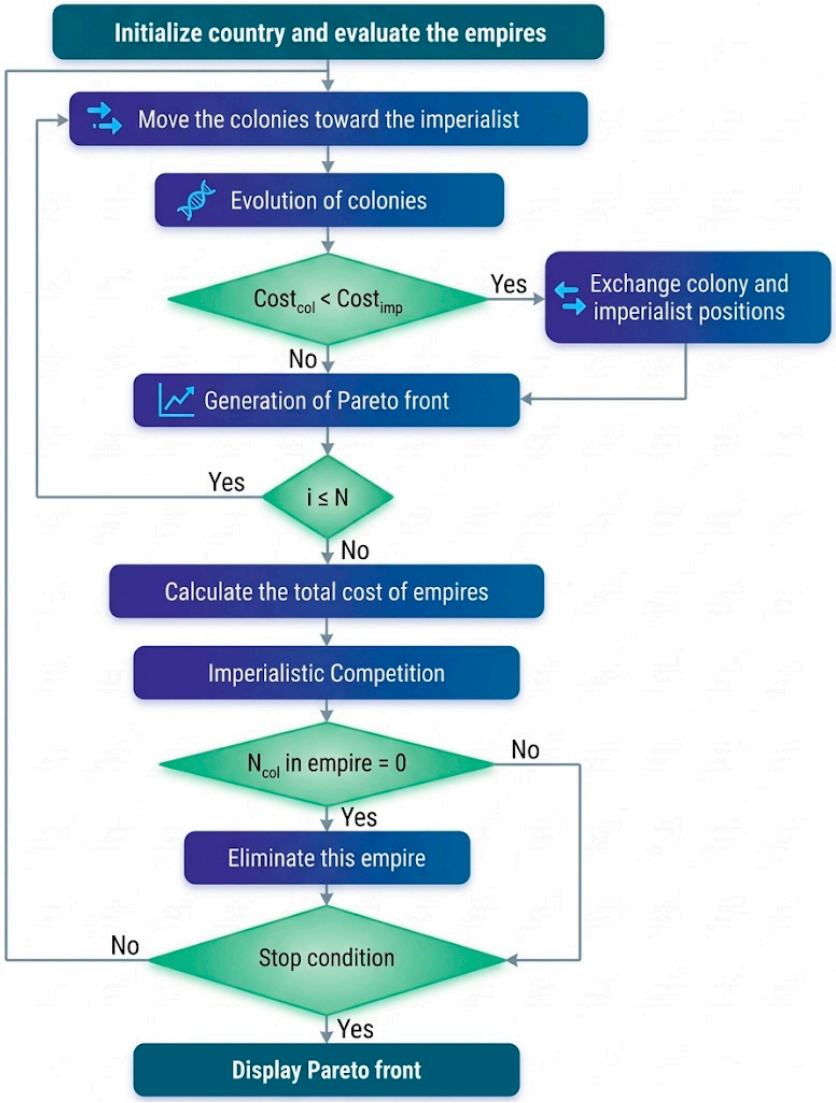


Figure 5. The MOICA steps.

Step 1: Initialization of Population and Empire Assessment

The MOICA framework initiates by generating a random set of "countries". In this energy supply application, each country serves as a design vector that contains a unique combination of design parameters; $[K_{pi}, K_{Ii}, K_{di}$, λi, μi, X, Y].

- Fitness Evaluation: The "cost" of each country is determined by assessing the objective functions: ITAE and ISC.
- Imperialist Selection: The individual with the lowest aggregate cost (indicating the best frequency regulation performance) is designated as an "imperialist," while the remaining individuals are labeled as "colonies".
- Cost Normalization: The relative strength of the nth imperialist is calculated using standardized formulas that account for the best, maximum, and minimum values of each objective function across the current iteration.

The normalized cost (Cn) and individual objective costs (Costn) are defined as follows [33,34]:

$$C_n = \max_i\{Cost_i\} - Cost_n \quad (18)$$

$$Cost_n = \sum_{j=1}^{r} \frac{\left| F_{j,n} - F_j^{best} \right|}{\left| F_j^{max} - F_j^{min} \right|} \tag{19}$$

In these expressions, r represents the total number of objective functions, and $F_{j,n}$ is the value of the j^{th} objective for the nth imperialist. The variables F_j^{best}, F_j^{max}, and F_j^{min} denote the optimal, peak, and lowest values observed for that specific objective during the iteration.

Step 2: Stochastic Assimilation and Adaptive Evolution Mechanisms

Following the establishment of initial empires, the MOICA executes a dual-phase optimization process to refine the control parameters for the energy supply system (see Figure 6).

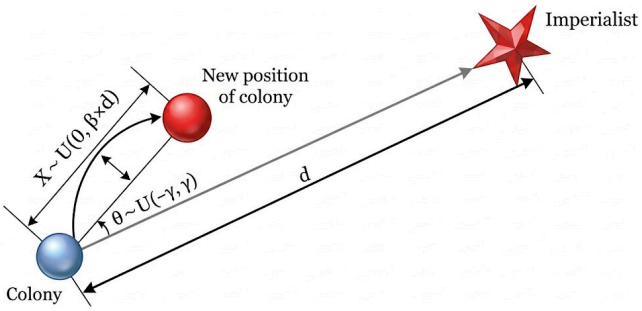


Figure 6. Stochastic Assimilation mechanism.

In the assimilation phase, colonies shift toward their respective imperialists based on a displacement distance X, drawn from a uniform distribution $U(0, \beta \times d)$, and a stochastic deviation angle (θ) from $U(-\gamma, \gamma)$, allowing for a comprehensive search around the current best solutions. To maintain population diversity and avoid local optima, a secondary stochastic evolution phase is implemented; this involves multi-point crossover to enhance convergence when the average colony-imperialist distance exceeds a threshold d_{max}, and random replacement mutation to introduce entirely new, high-power solutions if the distance falls below d_{min}.

Step 3: Pareto Front Archiving and Empire Cost Normalization

A critical phase in the MOICA framework involves the dynamic management of an external archive to track the evolving Pareto front of non-dominated imperialists. During the initial iteration, the algorithm assesses N imperialists using a fast-non-dominated sorting technique, where each candidate's objective functions (ITAE and ISC) are cross-compared to identify superior trade-offs. Those solutions not dominated by any other are preserved in the archive to establish the preliminary Pareto set. In all subsequent iterations, the classification process for new imperialists is streamlined by comparing their performance directly against the existing solutions within the archive rather than conducting an exhaustive cross-comparison of the entire population.

Following the update of the Pareto front, the aggregate cost of each empire within the energy supply model is calculated. The total cost of the nth empire (TCn) is defined by the performance of the imperialist and the average cost of its associated colonies, expressed as [17,30]:

$$TC_n = Cost_n + \xi mean(Cost_{col,n}) \tag{20}$$

In this equation, ξ serves as a scaling factor (ranging from 0 to 1) that modulates the influence of colonies on the empire's overall strength. A lower ξ minimizes the impact of colonies, whereas a higher value elevates their contribution to the empire's competitive

power. Finally, the normalized total cost (NTCn) is derived to rank the empires for the competitive phase [17,30]:

$$NTC_n = \max_i\{TC_i\} - TC_n \tag{21}$$

Step 4: Imperialistic Competition and Convergence Strategy

Following the calculation of the aggregate empire costs, the energy supply system optimization enters its final stage: the imperialistic competition. This phase represents a dynamic power struggle where empires vie for control over resources and colonies, a process visually detailed in Figure 7.

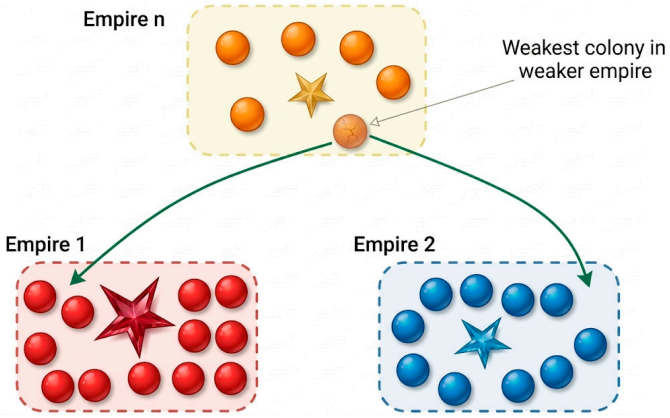


Figure 7. Competition between imperialists.

The core mechanics of this competitive stage are defined as follows:

- Colony Acquisition: Stronger, more dominant empires gradually seize colonies from their weaker counterparts.
- Possession Probability: The likelihood of an empire successfully capturing a new colony is determined by its calculated possession probability (Ppn), which is a ratio of its normalized total cost to the sum of costs across all empires [17,30]:

$$P_{p_n} = \left| \frac{NTC_n}{\sum_i NTC_i} \right| \tag{22}$$

- Empire Elimination: This competition creates a continuous cycle where powerful empires expand while weaker ones decline. Any empire that loses all its colonies is considered collapsed and is removed from the process.
- Termination Criteria: The MOICA concludes when the competitive landscape stabilizes into a single remaining empire, signifying that all less effective control configurations have been eliminated and the optimal parameters for the TTFOPID have been identified.

5. Optimization Results and Discussion

This section provides a thorough description of the Energy supply system simulations conducted within the MATLAB R2023b environment. A central component of the control architecture is the application of the MOICA to optimize the performance of the TTFOPID controllers. The comprehensive configuration of the energy supply system model utilized throughout these simulations is delineated in Figure 4. Hardware execution on an Intel® Core™ i7-1270P processor (16 GB RAM) yielded a rapid average runtime of 1.2 s and a memory requirement of less than 2 GB, confirming the algorithm's suitability for practical implementation.

The MOICA hyperparameters establish the computational framework for the optimization process, beginning with a total population of 1200 countries, from which the top 120 are designated as imperialists to lead the initial empires. The dynamics of the search space are governed by a share coefficient of $\xi = 0.01$ that accounts for the relative influence of colonies on an empire's total power. To maintain a robust balance between global exploration and local exploitation, the algorithm utilizes a high crossover probability of 0.8 to encourage the convergence of superior traits, while a mutation probability of 0.2 introduces stochastic variations to prevent the system from becoming trapped in local optima. This specific configuration ensures that the energy supply system's control parameters are refined with high precision while maintaining the diversity necessary to identify the most resilient FOPID settings.

5.1. Performance Comparison of MOICA-Optimized Controllers

In this experimental phase, the MOICA-optimized cascade (TTFOPID), standard FOPID, and conventional PID controllers are integrated into the energy supply system to evaluate their relative efficacy in attaining superior dynamic performance. Each control strategy is subjected to a 0.05 p.u. step load disturbance initiated at t = 1 s. The resulting Pareto fronts, which characterize the inherent trade-offs between the two conflicting objective functions (ITAE and ISC), are comparatively illustrated in Figure 8.

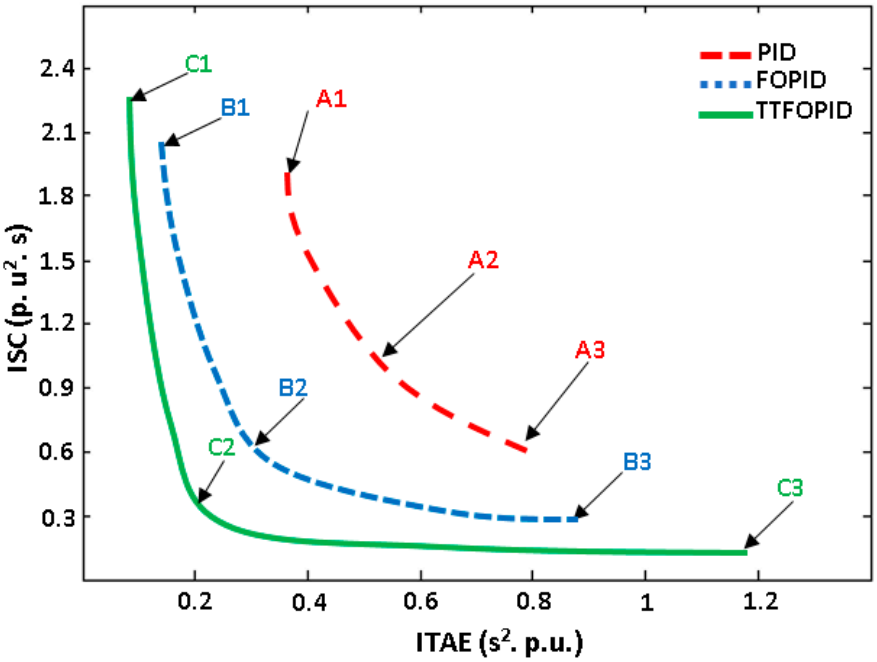


Figure 8. PID, FOPID and TTFOPID pareto fronts.

The Pareto front (presented in Figure 8) provides a comprehensive visual validation of the performance hierarchy between the three investigated control strategies: the TTFOPID, the standard FOPID, and the conventional PID. In multi-objective optimization, the proximity of a Pareto front to the origin (0,0) serves as the primary indicator of a controller's efficacy, as it represents the simultaneous minimization of the ITAE and ISC. The TTFOPID front clearly dominates the other two schemes by occupying the region closest to the origin. This suggests that the MOICA successfully leveraged the increased degrees of freedom inherent in the cascade fractional-order architecture to achieve a superior balance between frequency regulation accuracy and control energy conservation that neither the standard FOPID nor the PID could match.

To provide a more rigorous technical analysis of the results, specific non-dominated solutions are identified along the Pareto fronts, denoted as C1, C2, and C3. Solution C1 represents a high-performance configuration on the TTFOPID curve, where the ITAE is minimized to its lowest practical limit; this ensures a nearly instantaneous return to the nominal frequency, albeit at the expense of a higher control effort. In contrast, solution C2 illustrates a balanced operating point on the standard FOPID front; while it offers acceptable stability for the energy supply system, it remains significantly further from the ideal origin than its TTFOPID counterpart. Solution C3 is highlighted as the configuration providing the minimum ISC (Integral Square of Control signal) across the observed set. While C3 achieves this extreme reduction in control energy (thereby maximizing the longevity of the system's physical actuators) it simultaneously results in the highest ITAE, representing the most conservative approach to frequency regulation.

The transition between these selected solutions highlights the "Pareto optimal" trade-off governed by the MOICA method. Moving along the TTFOPID front from a point like C1 toward more conservative settings demonstrates how the algorithm can reduce the ISC to preserve actuator health while maintaining a level of ITAE that is still superior to the best possible PID response. This indicates that the TTFOPID provides a wider and more efficient operational range for the energy supply system. The clear separation between the fronts confirms that the series-connected fractional-order tiers allow for more precise "shaping" of the system's frequency response, effectively decoupling disturbance rejection from control signal volatility and providing the grid with enhanced dynamic resilience.

A quantitative breakdown of the representative optimal points extracted from the Pareto fronts in Figure 8 is provided in Table 3, offering a detailed performance assessment for each controller.

Table 3. Representative Pareto-Optimal Solutions.

		PID (i = 1)			**FOPID (i = 1)**			**TTFOPID (i = 1 & 2)**		
Solution		A1	A2	A3	B1	B2	B3	C1	C2	C3
ITAE		0.38	0.55	0.82	0.15	0.3	0.88	0.11	0.2	1.18
ISC		1.95	1.07	0.61	2.05	0.65	0.3	2.25	0.38	0.15
Design Parameters	K_{pi}	2.33	2.987	2.56	2.91	0.27	2.87	2.12/2.54	2.22/2.76	2.33/2.47
	K_{Ii}	0.44	2.993	0.57	2.62	2.965	2.38	2.35/2.25	2.88/2.63	2.67/2.48
	K_{di}	0.72	0.599	0.44	0.76	0.733	0.26	0.59/0.61	0.68/0.63	0.56/0.44
	λ_i	--	--	--	0.18	0.995	0.79	0.47/0.88	0.59/0.61	0.87/0.67
	μ_i	--	--	--	0.79	0.498	0.2	0.68/0.77	0.86/0.81	0.65/0.68
	X	8	10	8	9	8	8	8	9	9
	Y	2	2	4	4	2	2	10	10	4

Table 3 provides a quantitative validation of the Pareto-optimal trade-offs identified for the three control architectures, demonstrating that the TTFOPID configuration offers a superior performance envelope compared to the standard FOPID and conventional PID controllers. Across the nine representative solutions, a clear inverse relationship is observed between the ITAE and ISC metrics. In fact, solution C1 achieves the absolute minimum error (ITAE = 0.11) at the cost of the highest control effort (ISC = 2.25). However, C3 represents the most energy-efficient state with the lowest control signal intensity (ISC = 0.15). The data highlights the flexibility of the fractional-order parameters (λi, μi), which, when optimized by the MOICA, allow the TTFOPID to maintain significantly lower error-effort coordinates than the PID baseline (A1–A3).

To determine the optimal control configuration from the non-dominated Pareto front, the TOPSIS (Technique for Order of Preference by Similarity to Ideal Solution) approach is utilized. This method ranks each candidate by calculating its geometric distance to an ideal reference point through the closeness coefficient, defined as [39]:

$$C_{c_j} = \frac{d_j^-}{d_j^+ + d_j^-} \tag{23}$$

In this formulation, dj^+ denotes the geometric distance between the Pareto solution j and the ideal reference point, defined by the minimum values for both objectives ($ITAE_{min}$ and ISC_{min}). Conversely, dj^- signifies the distance between solution j and the non-ideal reference point, which comprises the worst objective values observed across the front ($ITAE_{max}$ and ISC_{max}).

Based on the TOPSIS method, the most effective configurations are identified as C2 for TTFOPID, B2 for FOPID, and A2 for PID fronts. While solutions like C1 and C3 prioritize a single objective, the TOPSIS-selected C2 provide the most stable and efficient performance for the energy supply system by maximizing the trade-off efficiency on their respective Pareto fronts.

In all subsequent analyses, the TTFOPID, FOPID, and PID controllers will be evaluated using their most effective configurations (C2, B2, and A2, respectively).

5.2. Frequency-Domain Stability Analysis

The dynamic performance of each controller is further assessed in the frequency domain.

The Bode plot frequency response of the system, illustrated in Figure 9, compares the PID (A2), FOPID (B2), and the Proposed TTFOPID (C2) configurations. In the magnitude plot, the TTFOPID exhibits a significantly higher gain in the low-frequency region (10^{-3} to 10^{-1} rad/s) compared to its counterparts. This elevated low-frequency magnitude is a critical technical advantage, as it directly correlates to superior steady-state tracking and more robust rejection of load disturbances, ensuring the energy supply system maintains nominal frequency under varying conditions.

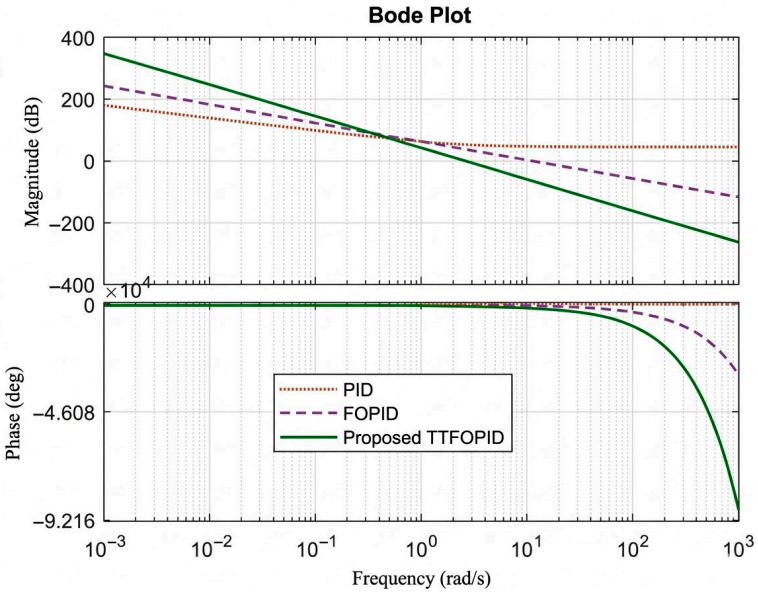


Figure 9. Bode Analysis of PID, FOPID, and TTFOPID Controllers.

As the frequency increases toward the 0 dB crossover point, the TTFOPID demonstrates a steeper roll-off rate than the standard FOPID and PID controllers. While all three strategies converge near the unit gain crossover frequency, the TTFOPID provides much sharper attenuation in the high-frequency range. This characteristic is particularly beneficial for system longevity and reliability. In fact, TTFOPID effectively filters out high-frequency measurement noise and prevents volatile oscillations from reaching the physical actuators, thereby justifying the lower ISC values observed in the previous Pareto analysis.

Regarding the phase response, the TTFOPID introduces a more pronounced phase lag at higher frequencies compared to the simpler control architectures. However, as shown in Figure 9, both the gain and phase margins remain positive across a wide frequency range, satisfying the classical frequency-domain stability criteria. This confirms that the closed-loop system is asymptotically stable and that the TTFOPID structure allows precise "loop shaping." Ultimately, this architecture successfully decouples high-gain performance at low frequencies from noise immunity at high frequencies (a feat that the traditional PID cannot achieve due to its structural simplicity).

The Nyquist plot (in Figure 10) provides a comprehensive assessment of the absolute and relative stability of the energy supply system under the PID, FOPID, and Proposed TTFOPID control schemes. By mapping the open-loop frequency response onto the complex plane, the plot illustrates the relationship between the real and imaginary components as frequency varies. Crucially, none of the trajectories encircle the critical point $(-1, 0)$, which is highlighted by a black cross in the inset view. This absence of encirclement confirms that all three control configurations satisfy the Nyquist stability criterion, ensuring that the system remains asymptotically stable.

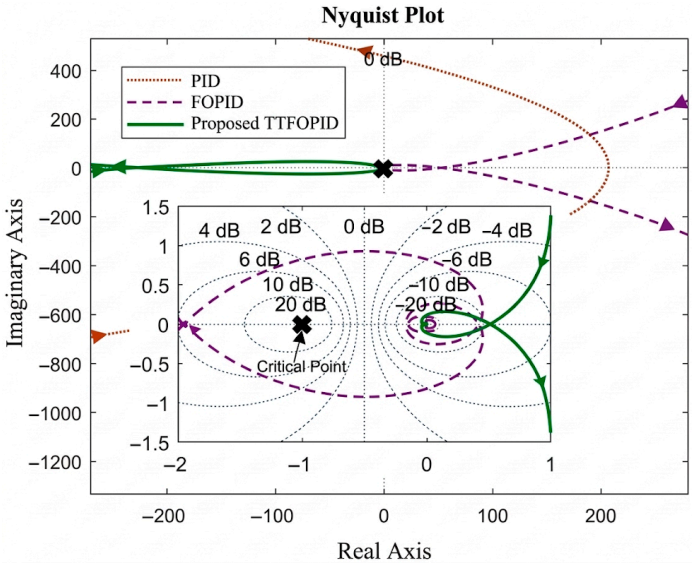


Figure 10. Comparative Frequency-Domain Stability Analysis using Nyquist Plots.

Moreover, the TTFOPID trajectory maintains a significant distance from the $(-1, 0)$ point, suggesting a robust phase and gain margin. In contrast, the FOPID and PID plots show different sensitivities to frequency changes. The clear separation between the trajectories near the critical point indicates that the TTFOPID provides a better safety buffer against system parameter variations or uncertainties. This physical distance in the complex plane translates to the "dynamic resilience" mentioned in the time-domain analysis, where the controller can reject disturbances without risking instability.

Furthermore, the Nyquist plot validates the loop-shaping capabilities of the fractional-order architectures. While the PID follows a more conventional path, the TTFOPID architecture exhibits a unique curvature that reflects its increased degrees of freedom. By strate-

gically positioning the polar plot further away from the instability region, the TTFOPID achieves a superior balance between high performance and robust stability. This visual evidence complements the Bode plot findings, proving that the proposed TTFOPID structure not only optimizes error metrics like ITAE but also ensures a more secure operational envelope for the energy supply system.

5.3. Performance Analysis Under Stochastic Solar Irradiance and Load Disturbances

To evaluate the robustness of the proposed control strategies under realistic operating conditions, the energy supply system is subjected to a time-varying disturbance profile. Figure 11 illustrates the normalized solar irradiance and the corresponding photovoltaic (PV) output power utilized for this study. This profile represents the inherent intermittency of renewable energy sources, characterized by rapid fluctuations and unpredictable power drops, which serve as a rigorous dynamic test for the TTFOPID, FOPID, and PID controllers within the integrated energy network.

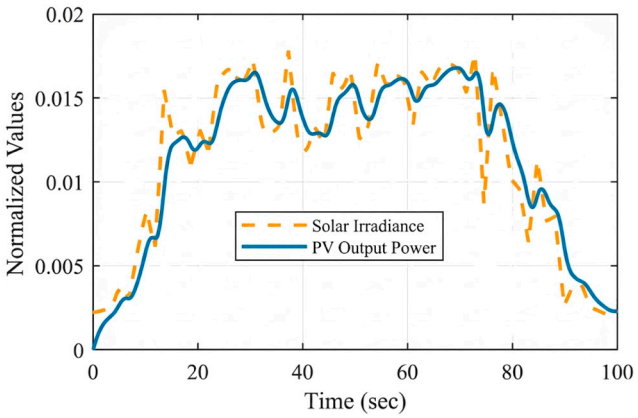


Figure 11. Solar Irradiance and PV Power Disturbance Profile.

The impact of these solar power variations on the stability of the energy supply system is depicted through the frequency deviation in Figure 12 and the BESS power exchange in Figure 13. It should be noted that in this standalone configuration, 'power exchange' refers to the dynamic compensation provided by the BESS to balance the fluctuations between renewable generation and local load demand, rather than grid-level tie-line exchange.

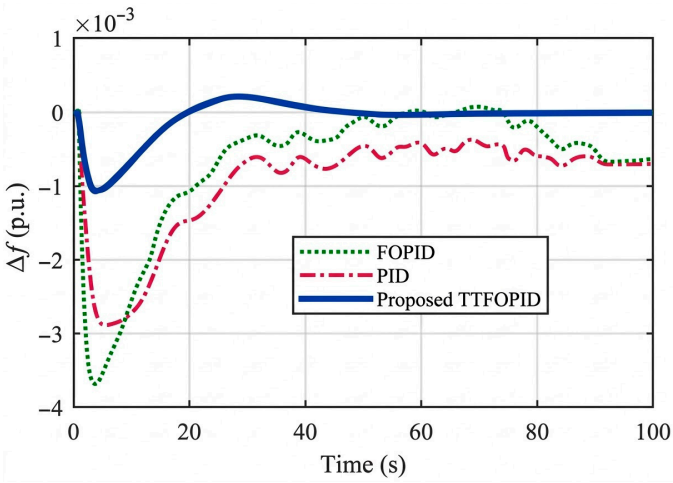


Figure 12. Frequency Response Comparison for PID, FOPID and TTFOPID.

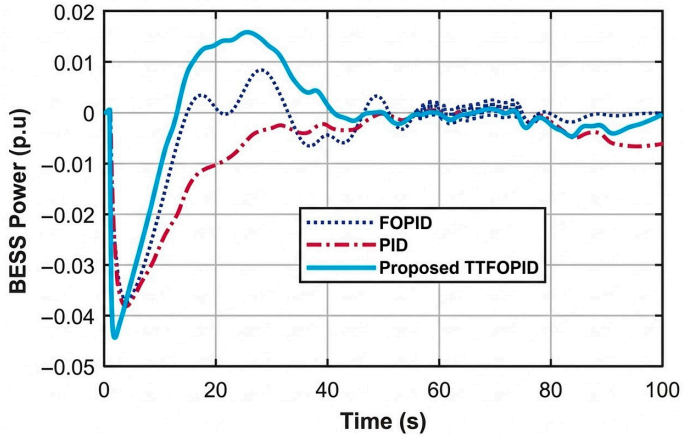


Figure 13. Dynamic power response of the BESS under solar irradiance fluctuations (PV disturbance).

Figure 12 illustrates the dynamic response of frequency deviation (Δf), comparing the performance of the PID, FOPID, and Proposed TTFOPID controllers. The transient response clearly shows that the TTFOPID significantly outperforms the other two configurations in terms of damping and speed of recovery. While the PID and FOPID controllers exhibit deep frequency nadirs and prolonged oscillations, the TTFOPID controller successfully limits the initial drop and quickly stabilizes the system, demonstrating its superior ability to maintain grid frequency within narrow operational limits. Theoretically, this is attributed to the fact that the TTFOPID's fractional derivative tier provides a faster 'kick' during the initial error phase while the fractional integrator tier ensures a smoother return to steady-state without the excessive overshoot typically seen in high-gain integer-order cascade systems.

These results reveal that the TTFOPID provides the necessary flexibility to handle nonlinearities more effectively than traditional integer-order or standard fractional-order controllers. As observed in the plot, both the PID and FOPID controllers suffer from significant undershoot and a "ringing" effect, where the frequency struggles to return to zero. In contrast, the TTFOPID response is much smoother and achieves a near-zero steady-state error in a fraction of the time, which is vital for preventing the triggering of under-frequency load shedding relays in real-world power systems.

To further quantify these dynamic improvements, Table 4 summarizes the key performance characteristics extracted from the frequency fluctuation.

Table 4. Comparison of Dynamic Performance Specifications.

Controller	Peak Undershoot (p.u.)	Settling Time (s)	Steady-State Error	Oscillation Damping
PID	-2.9×10^{-3}	>100	Moderate Residual	Poor
FOPID	-3.7×10^{-3}	>100	Low Residual	Moderate
TTFOPID	-1.1×10^{-3}	40	Zero	Excellent

Figure 13 illustrates the power response of the BESS as it compensates for the fluctuations in solar irradiance and PV output power. In the context of the energy supply system, the BESS acts as a fast-acting buffer, injecting or absorbing power to maintain the frequency balance.

One can note that the TTFOPID controller commands a much more precise and well-damped power response from the BESS. While the PID and FOPID controllers lead to larger and more volatile power swings along with persistent oscillations, the TTFOPID ensures that the BESS responds efficiently to the primary disturbance. This behavior indicates that the two-tier fractional-order logic better coordinates the energy storage assets. It provides exactly the amount of power needed to cancel the PV intermittency without overstress-

ing the system, which optimizes both frequency stability and the operational lifespan of the BESS.

The superiority of the TTFOPID over conventional FOPID is largely attributed to the multiplicative interaction between the two tiers. In the frequency domain, this structure allows for a more complex pole-zero placement. The first tier provides the necessary phase lead to improve the system's response speed, while the second tier ensures that the control effort (ISC) is minimized by dampening high-frequency oscillations. This synergistic effect, optimized via MOICA, results in a deeper stability margin and faster settling time compared to additive fractional-order controllers.

6. Validation of MOICA-Tuned TTFOPID: From Comparative Benchmarking to Robustness Evaluation

6.1. Benchmarking MOICA-Tuned TTFOPID: Comparative Performance

To validate the efficacy of the MOICA in optimizing the TTFOPID controller, a comparative study is conducted against several established meta-heuristic techniques. Specifically, we compare the obtained optimal Pareto front solutions (optimized for the contradictory objectives of minimizing ITAE and ISC) with TTFOPID controllers tuned using other common multi-objective algorithms, NSGAII and MOPSO. The performances are evaluated under the load disturbances presented in Figure 14.

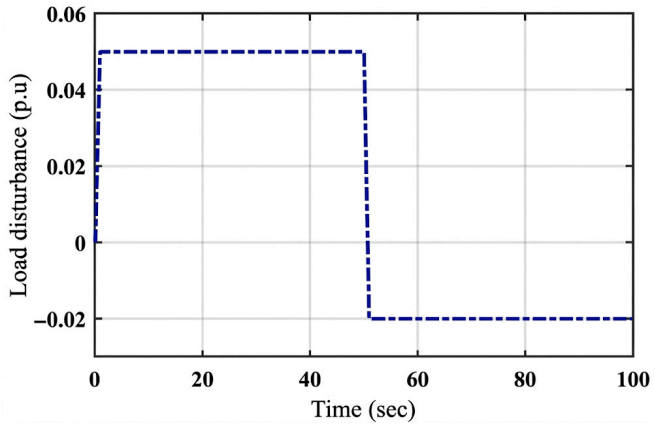


Figure 14. Load Disturbance Profile.

Figure 15 represents the multi-objective Pareto front distribution for the TTFOPID controller parameters tuned using three different optimization algorithms. The figure plots the trade-off between two conflicting objectives: ITAE, which represents system tracking performance and settling time, and ISC, which measures the control effort and energy consumption.

The results in Figure 15 highlight the clear superiority of the MOICA-tuned TTFOPID controller. Its Pareto front is positioned closest to the origin, confirming that it simultaneously achieves a lower tracking error (ITAE) and reduced control effort (ISC) compared to its competitors. In contrast, the solutions provided by NSGA-II and MOPSO are situated further to the right and top of the objective space, indicating that they require either a higher control cost to achieve the same precision or result in greater system error for the same energy expenditure.

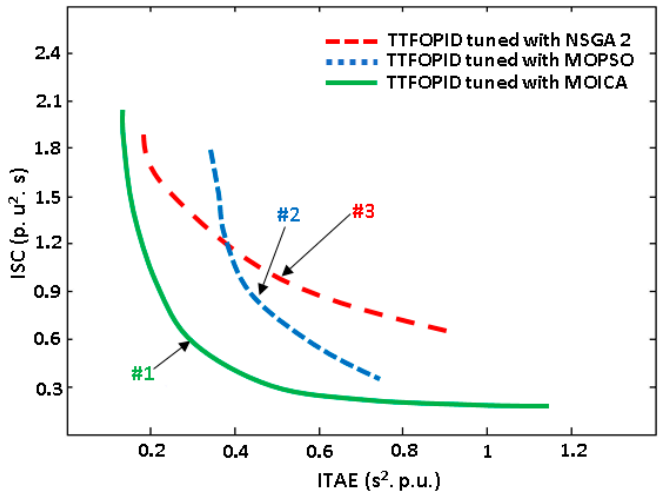


Figure 15. Pareto Fronts of TTFOPID tuned with different algorithms. Points #1, #2, and #3 represent the final compromise design solutions selected from the Pareto front of each respective optimization method.

The MOICA front also exhibits a wider and more continuous distribution of non-dominated solutions. This diversity allows for a more flexible selection of optimal operating points, such as point #1, which offers an ideal balance by minimizing both frequency overshoot and battery wear. To quantify the superiority of the proposed method, Table 5 compares specific coordinates along the Pareto fronts to determine the percentage of improvement.

Table 5. Quantitative Comparison of Pareto Front Objectives.

Comparison Point	MOICA	NSGA-II	Improvement % (MOICA vs. NSGA-II)	MOPSO	Improvement % (MOICA vs. MOPSO)
ISC values at ITAE = 0.4	0.42	1.25	66.4%	0.95	55.8%
ITAE values at ISC = 0.6	0.25	0.90	72.2%	0.58	56.9%
ITAE values at ISC = 0.9	0.19	0.52	63.5%	0.45	57.8%

For comparison reasons, the most effective configurations (Based on the TOPSIS method) are identified as #1 for TTFOPID, #2 for MOPSO, and #3 for NSGA2. A quantitative breakdown of the #1, #2and #3 solutions is provided in Table 6.

Table 6. The most effective configurations Pareto-Optimal Solutions.

		MOICA	MOPSO	NSGAII
Solution		#1	#2	#3
ITAE		0.29	0.45	0.52
ISC		0.59	0.87	1.01
Design Parameters (i = 1, 2)	K_{pi}	2.18/2.79	2.02/2.13	2.11/2.21
	K_{Ii}	2.11/2.88	2.12/2.03	2.77/2.32
	K_{di}	0.57/0.45	0.42/0.39	0.35/0.66
	λ_i	0.49/0.61	0.51/0.65	0.91/0.39
	μ_i	0.78/0.69	0.57/0.78	0.63/0.66
	X	9	1	1
	Y	10	8	4

To account for the stochastic nature of the metaheuristic optimization algorithms (MOICA, NSGA-II, and MOPSO), each algorithm was executed for 30 independent simulation runs. At each run, the values of ITAE and ISC for solutions #1, #2 and #3 have been recorded. This ensures that the results are statistically significant and not the product of a single advantageous initialization. Table 7 presents the statistical comparative analysis of the objective functions obtained over 30 runs.

Table 7. Statistical Performance Comparison (30 Independent Runs).

Objective	Algorithm	Best (Min)	Mean	Worst (Max)	Standard Deviation
ITAE	MOICA	0.287	0.291	0.334	0.011
	NSGA-II	0.453	0. 522	0.655	0.058
	MOPSO	0.384	0.451	0.553	0.056
ISC	MOICA	0. 573	0.592	0.629	0.012
	NSGA-II	0.985	1.017	1.196	0.052
	MOPSO	0.722	0.865	1.013	0.073

Furthermore, the boxplot in Figure 16 illustrates the distribution of the results for ITAE and ISC. One can note the clear vertical separation and lack of overlap between the MOICA distribution and those of the competing algorithms, which establishes the absolute statistical dominance of the proposed method. The compressed height of the MOICA box signifies a remarkably low standard deviation, demonstrating that the algorithm is highly robust and consistently converges to nearly identical high-quality solutions across multiple independent runs. Furthermore, the positioning of the mean line close to the minimum value indicates a favorable positive skew, confirming that the algorithm efficiently identifies the global optimum rather than becoming trapped in local minima. This high concentration of optimal results proves that the TTFOPID controller tuned via MOICA not only achieves significantly lower ITAE and ISC but does so with a level of stochastic reliability that is essential for practical engineering applications in Energy supply system.

The optimal #1, #2 and #3 solutions are subsequently used to analyze the frequency fluctuations, control signals, and BESS power responses of the TTFOPID controller when tuned by different algorithms.

Figure 17 displays the frequency deviation of the energy supply system over a 100 s interval. It compares the TTFOPID controller performance when tuned using three different multi-objective algorithms: MOICA, NSGA-II, and MOPSO. The system is subjected to load disturbances at t = 0 s and t = 50 s as shown in the load profile (Figure 14).

The response illustrates the dynamic stability of the power system. At t = 0 s, a load increase triggers an initial frequency drop. While all three controllers attempt to restore the frequency to the nominal value (0 p.u.), they exhibit different damping characteristics. At t = 50 s, a second load change occurs, creating a transient phase that highlights the differences in peak deviation and settling behavior. The MOICA-tuned TTFOPID consistently provides the most stable profile. It features the smallest deviations and the most effective damping of oscillations. While NSGA-II has a slightly lower initial overshoot at the 50 s mark, it suffers from severe secondary oscillations and a large frequency dip near 75 s. MOPSO exhibits the largest peak overshoot and persistent fluctuations.

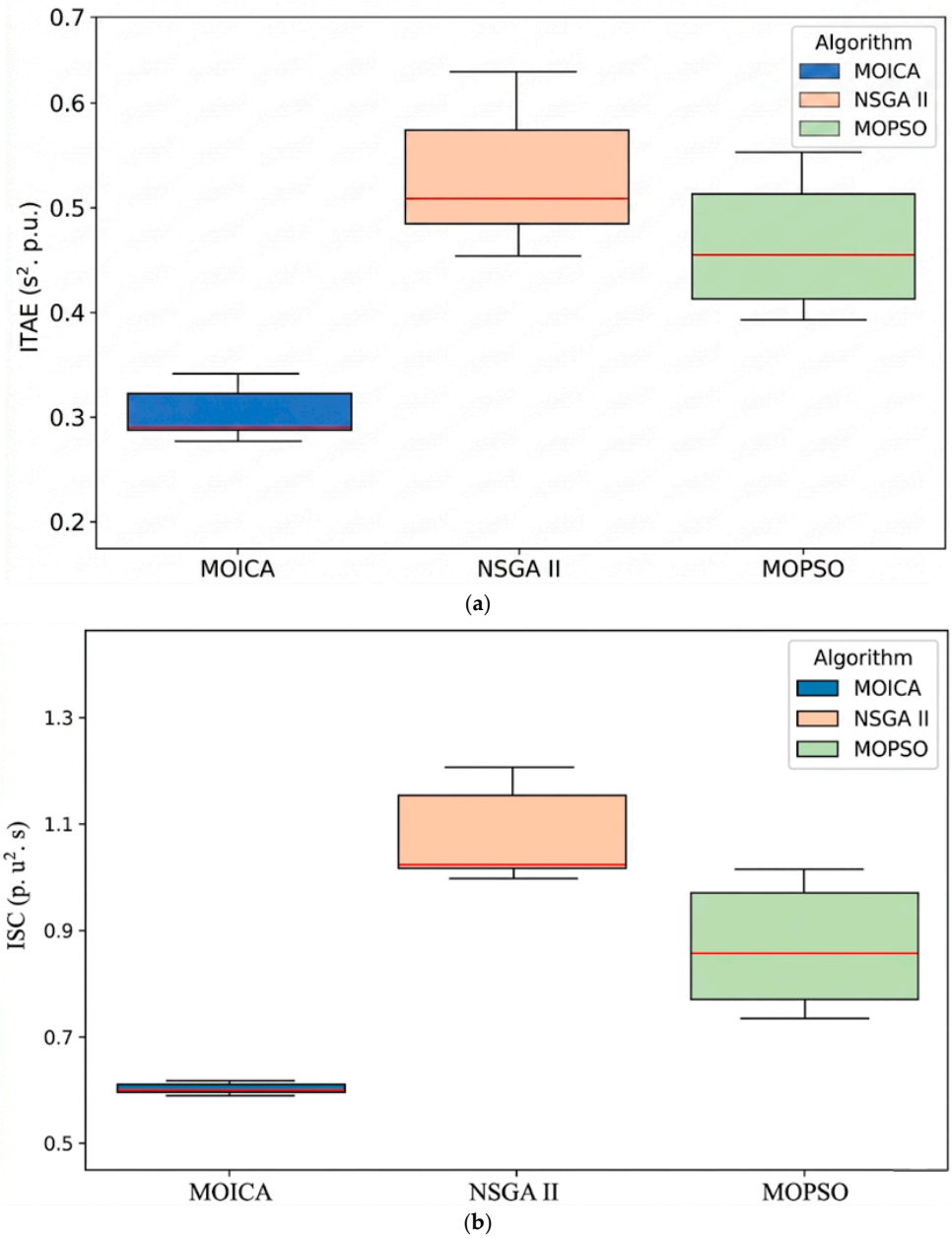


Figure 16. Box Plot of ITAE and ISC Comparison for different algorithms. (**a**) ITAE comparison, (**b**) ISC comparison.

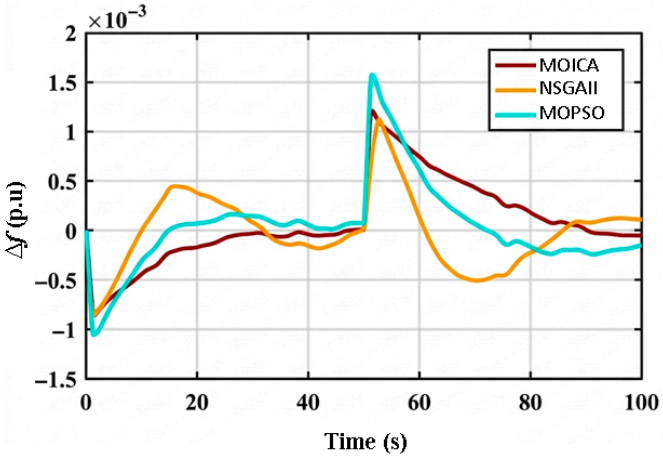


Figure 17. Comparative Analysis of System Frequency Fluctuations for Various Tuning Methods.

Table 8 presents the performance values for various tuning methods.

Table 8. Performance values for different tuning Methods.

Performance Metric (p.u.)	MOICA	NSGA-II	MOPSO
Max. Undershoot	-0.85×10^{-3}	-0.90×10^{-3}	-1.05×10^{-3}
Max. Overshoot	1.22×10^{-3}	1.15×10^{-3}	1.60×10^{-3}
Settling Time	85	>100	>100

The numerical data confirms that the MOICA provides the superior parameter tuning for the TTFOPID controller. By minimizing the peak deviations and eliminating persistent oscillations, MOICA ensures a faster return to steady-state. This reduces the mechanical and electrical stress on the energy supply system assets.

Figure 18 illustrates the control signal generated by the TTFOPID controller across the 100 s simulation period. This signal represents the physical effort exerted by the controller to mitigate the load disturbances introduced at 0 s and 50 s. During the initial transient phase from 0 to 50 s, all signals move into negative territory to compensate for the load increase. While NSGA-II exhibits an aggressive and oscillatory response, MOICA follows a much smoother and well-damped trajectory. Following the second load change at 50 s, the control signals surge upward, where NSGA-II shows a significant overshoot peaking near 0.06 p.u. and MOPSO peaks at approximately 0.04 p.u., whereas MOICA remains the most conservative, peaking at roughly 0.025 p.u.

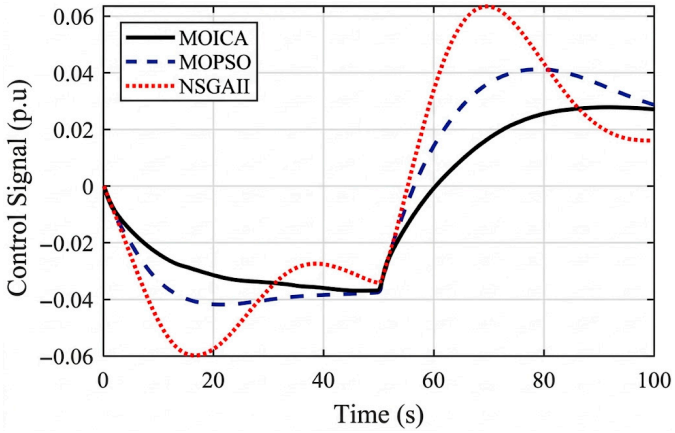


Figure 18. Comparative Analysis of System Control signal for different tuning Methods.

The interpretation of these results is a direct reflection of the ISC metric. In practical power system applications, a superior control signal is one that is smooth and minimizes peak values, as sharp spikes and high-frequency oscillations cause mechanical wear and tear while rapidly depleting battery reserves. As presented in Figure 18, MOICA achieves the lowest peak signal of approximately 0.028 p.u. with high smoothness, resulting in minimal control effort. In contrast, MOPSO demonstrates moderate effort with a peak of 0.042 p.u., and NSGA-II shows the highest effort and lowest smoothness, peaking at 0.063 p.u. with high oscillations.

In conclusion, the MOICA-tuned controller demonstrates superior efficiency by achieving better frequency regulation while using significantly less control effort. The absence of oscillations in the MOICA signal indicates that the two-tier fractional-order parameters have been optimized to provide a "soft" yet highly effective response. This characteristic is critical for real-world implementation, as it directly extends the lifespan of the power system's actuators and energy storage components by reducing unnecessary stress on the infrastructure.

6.2. Robustness of the Optimal Solutions Under Parameter Uncertainty

This analysis investigates the impact of system parameter variations on the optimal solution (#1) across three critical operational scenarios commonly encountered in energy supply systems:

Scenario A: Evaluation of Sensitivity to Power System Gain (Kp)

The power system gain, Kp, is a vital parameter representing the relationship between power imbalances and frequency deviations, acting as the inverse of the system's damping characteristic. In Energy supply system, this parameter fluctuates due to the changing nature of connected loads and varying self-regulation from different electrical appliances. By varying Kp from its nominal value of 1.0 to 0.5 and 1.5, this scenario verifies if the MOICA-tuned TTFOPID controller maintains stability across both highly sensitive and heavily damped grid conditions.

Figure 19 demonstrates the robustness of the TTFOPID controller tuned by MOICA under significant variations in the power system gain, Kp. As observed in the transient response curves, despite the Kp value being tripled across the scenarios, the frequency deviation (Δf) remains remarkably stable. While a higher gain typically makes a system more prone to instability or aggressive ringing, the MOICA-tuned parameters ensure that the frequency nadir and the recovery trajectory stay within a very tight, acceptable margin.

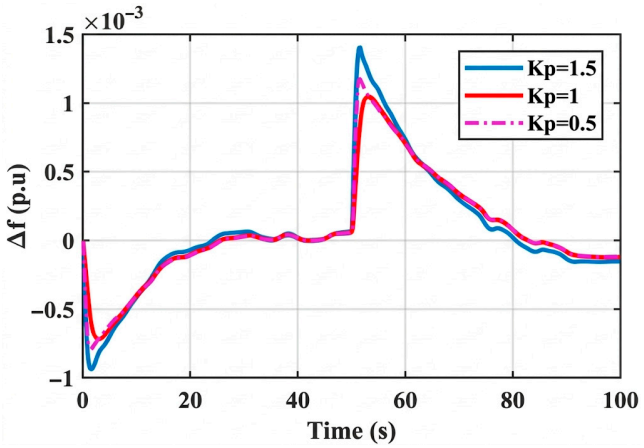


Figure 19. Sensitivity of TTFOPID to Power System Gain (Kp) variations.

The most critical evidence of robustness is the consistent return to the nominal frequency. In all three cases, the controller successfully eliminates the steady-state error, bringing Δf back to zero without exhibiting any growing oscillations or sustained instability. This indicates that the TTFOPID structure, when optimized by the MOICA, possesses a high degree of "parametric insensitivity." This means the controller does not rely on a perfect mathematical model of the grid to function effectively; rather, it maintains a superior stability margin that can handle the unpredictable nature of load-damping changes in a standalone microgrid.

Furthermore, the smoothness of the recovery across all Kp variations suggests that the control effort is well-distributed. Even when the system sensitivity is at its peak (Kp = 1.5), the MOICA-tuned TTFOPID prevents the sharp, high-frequency "chatter" often seen in standard PID controllers under high gain. This result validates that the proposed optimization strategy effectively navigates the complex search space to find a solution that is not only optimal for a single point but is also resilient to the modeling uncertainties and aging effects that characterize real-world energy supply systems.

Scenario B: Assessment of Robustness Against Governor Time Constant (Tg) variations

The governor time constant, Tg, determines how quickly the primary mover adjusts mechanical power output in response to control signals. Over time, mechanical wear, aging components, or fuel quality changes can cause significant response delays. This scenario evaluates controller performance at Tg values of 0.05 s, 0.1 s, and 0.15 s to demonstrate that the proposed optimization ensures the system remains stable and oscillation-free, even when mechanical hardware slows beyond its original design specifications.

Figure 20 illustrates the robustness of the TTFOPID controller tuned by MOICA when subjected to significant variations in the governor time constant, Tg. As observed in the frequency deviation (Δf) curves, although the mechanical delay is tripled from the fastest to the slowest scenario, the controller maintains a highly stable and consistent performance profile. While a larger time constant naturally introduces a slightly deeper initial frequency dip due to the slower injection of power, the MOICA-tuned parameters ensure that these deviations remain well within safe operational limits.

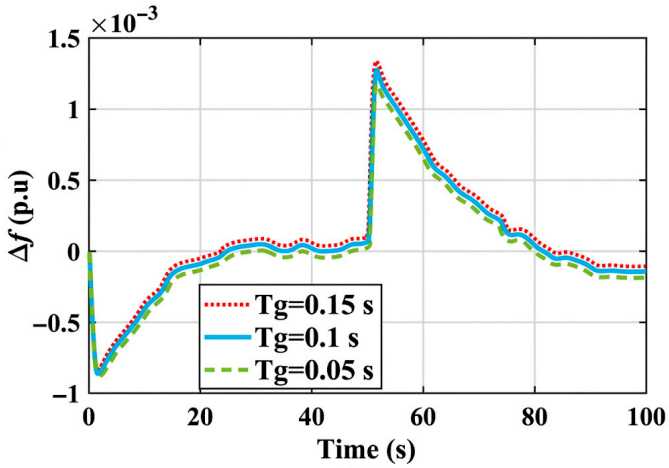


Figure 20. Sensitivity of TTFOPID to Governor Time Constant (Tg) variations.

The evidence of robustness is further underscored by the controller's ability to suppress oscillations across all three cases of Tg. Despite the increased phase lag introduced by a higher Tg, which typically threatens the stability margin of standard controllers, the MOICA-optimized TTFOPID maintains a smooth recovery trajectory. There is no evidence of sustained ringing or instability, and the system successfully returns to the nominal frequency in every instance. This proves that the fractional-order integral and derivative terms have been tuned to provide a high level of damping that is resilient to the slowing of mechanical hardware, ensuring that the microgrid remains reliable even as components degrade over time.

In conclusion, the results depicted in Figure 20 validate that the MOICA identifies a globally robust parameter set rather than one tailored strictly to nominal conditions. By maintaining a near-identical settling behavior even when the governor's responsiveness is significantly compromised, the controller demonstrates its suitability for real-world energy supply systems. This "parametric immunity" to Tg fluctuations ensures that the standalone microgrid can tolerate the inherent uncertainties of mechanical systems while providing high-quality frequency regulation and protecting sensitive equipment from large transients.

Scenario C: Impact of BESS Parameter Uncertainty (R_{BESS})

In modern energy supply system, the BESS provides essential fast-acting frequency regulation, governed by the droop or resistance parameter R_{BESS}. This parameter varies based on the battery's State of Charge (SOC), temperature, and long-term chemical degradation. By testing the controller under R_{BESS} values of 0.1, 0.2, and 0.3, this scenario simulates different stages of battery health.

The results illustrated in Figure 21 evaluate the sensitivity of the proposed control system to variations in the BESS droop parameter, R_{BESS}. Despite tripling the R_{BESS} value, the variations in the frequency nadir remain remarkably minimal, indicating a high degree of resilience against uncertainties within the energy storage units.

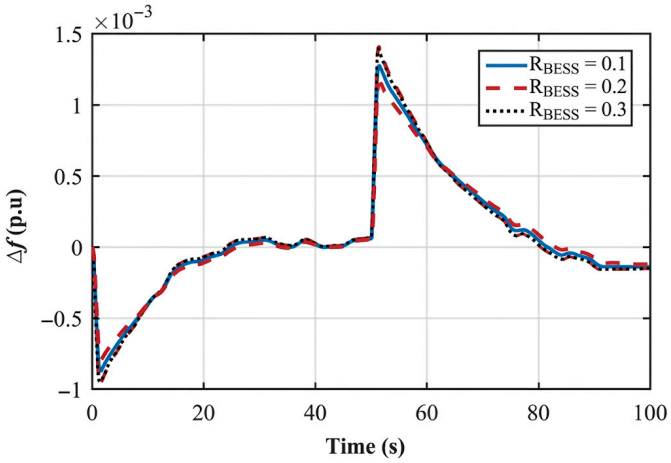


Figure 21. Sensitivity of TTFOPID to BESS resistant Parameter (R_{BESS}) variations.

A primary indicator of the MOICA-tuned controller's robustness is the consistency of the frequency recovery and the stability of the settling time across all scenarios. While increasing R_{BESS} typically slows down the battery's contribution to frequency regulation, the fractional-order architecture successfully compensates for this delay through its precisely tuned parameters, preventing secondary swings or system instability. The controller's ability to drive the frequency deviation back to zero promptly and with a well-damped trajectory confirms that the optimal solutions provided by MOICA are robust enough to handle the varying and realistic operational conditions of an energy supply system.

This 'parametric immunity' across varying hardware states serves as a critical simulation-based validation of the controller's real-world feasibility. By maintaining stability under significant parametric shifts, the TTFOPID demonstrates it can handle the non-ideal conditions often found in physical experimental setups.

In conclusion, these results reinforce the reliability of applying the TTFOPID controller in autonomous power systems, where consistent performance despite R_{BESS} fluctuations. The study proves that the combination of an advanced controller structure and a powerful optimization algorithm provides a dual layer of protection against both external load disturbances and internal parameter variations. This establishes the proposed system as a dependable and practical solution for the frequency stability challenges inherent in modern smart energy supply system.

7. Conclusions

This study established a multi-objective optimization framework for enhancing frequency stability in standalone energy supplies via an original Two-Tier Fractional-Order PID (TTFOPID) controller. By employing a dual-loop structure, the proposed architecture effectively decouples fast solar-converter transients from the slower dynamics of mechanical generators and battery storage. The implementation of the MOICA, enhanced with attractive and repulsive assimilation phases, proved superior in identifying the optimal Pareto-front within a high-dimensional parameter space.

A key contribution of this work is the simultaneous tuning of low-level controller gains and high-level hardware parameters, such as BESS sizing and droop settings. Quantitative validation confirmed that the MOICA-tuned TTFOPID achieved a 72% improvement in the

ITAE index compared to NSGA-II and a 56% improvement in the ISC index over MOPSO. Furthermore, the proposed system demonstrated 'parametric immunity,' maintaining stability under significant uncertainties in system gain, time constants, and battery parameter. This holistic strategy ensures resilient frequency recovery and protects the actuator under stochastic load disturbances.

While the present study provides a simulation-based validation using experimentally grounded models, future work will focus on implementing the TTFOPID-MOICA framework on a hardware-in-the-loop (HIL) testbed to further evaluate its performance under real-time computational constraints and hardware nonlinearities.

Author Contributions: Conceptualization, M.N.; Methodology, A.A.; Software, A.A.; Validation, M.N.; Writing—original draft, A.A.; Writing—review & editing, M.N.; Supervision, A.A. All authors have read and agreed to the published version of the manuscript.

Funding: This research received external funding from the Deanship of Graduate Studies and Scientific Research at Qassim University (QU-APC-2026).

Data Availability Statement: All data that support the findings of this study are included within the article.

Acknowledgments: The Researchers would like to thank the Deanship of Graduate Studies and Scientific Research at Qassim University for financial support (QU-APC-2026).

Conflicts of Interest: The authors declare no conflicts of interest.

References

1. Miller, M.; Yokwana, X.; Sumbwanyambe, M. Evaluating the Role of Hybrid Renewable Energy Systems in Supporting South Africa's Energy Transition. *Processes* **2025**, *13*, 3455. [CrossRef]
2. Saleh, A.M.; Vokony, I.; Waseem, M.; Khan, M.A.; Al-Areqi, A. Power system stability with high integration of RESs and EVs: Benefits, challenges, tools, and solutions. *Energy Rep.* **2025**, *13*, 2637–2663. [CrossRef]
3. Korovushkin, V.; Boichenko, S.; Artyukhov, A.; Ćwik, K.; Wróblewska, D.; Jankowski, G. Modern Optimization Technologies in Hybrid Renewable Energy Systems: A Systematic Review of Research Gaps and Prospects for Decisions. *Energies* **2025**, *18*, 4727. [CrossRef]
4. Maghami, M.R.; Mutambara, A.G.O. Challenges associated with Hybrid Energy Systems: An artificial intelligence solution. *Energy Rep.* **2023**, *9*, 924–940. [CrossRef]
5. Ahmad, S.; Hasan, S.M.N.; Hossain, M.S.; Uddin, R.; Ahmed, T.; Mustayen, A.G.M.B.; Hazari, M.R.; Hassan, M.; Parvez, M.S.; Saha, A. A Review of Hybrid Renewable and Sustainable Power Supply System: Unit Sizing, Optimization, Control, and Management. *Energies* **2024**, *17*, 6027. [CrossRef]
6. Elalfy, D.A.; Gouda, E.; Kotb, M.F.; Bureš, V.; Sedhom, B.E. Comprehensive review of energy storage systems technologies, objectives, challenges, and future trends. *Energy Strategy Rev.* **2024**, *54*, 101482. [CrossRef]
7. Juma, M.I.; Mwinyiwiwa, B.M.M.; Msigwa, C.J.; Mushi, A.T. Design of a Hybrid Energy System with Energy Storage for Standalone DC Microgrid Application. *Energies* **2021**, *14*, 5994. [CrossRef]
8. Badrudeen, T.U.; Nwulu, N.I.; Gbadamosi, S.L. Low-inertia control of a large-scale renewable energy penetration in power grids: A systematic review with taxonomy and bibliometric analysis. *Energy Strategy Rev.* **2024**, *52*, 101337. [CrossRef]
9. Rajendran, G.; Raute, R.; Caruana, C. A Comprehensive Review of Solar PV Integration with Smart-Grids: Challenges, Standards, and Grid Codes. *Energies* **2025**, *18*, 2221. [CrossRef]
10. Gulzar, M.M.; Sibtain, D.; Alqahtani, M.; Alismail, F.; Khalid, M. Load frequency control progress: A comprehensive review on recent development and challenges of modern power systems. *Energy Strategy Rev.* **2025**, *57*, 101604. [CrossRef]
11. Wu, D.; Guo, F.; Yao, Z.; Zhu, D.; Zhang, Z.; Li, L.; Du, X.; Zhang, J. Enhancing Reliability and Performance of Load Frequency Control in Aging Multi-Area Power Systems under Cyber-Attacks. *Appl. Sci.* **2024**, *14*, 8631. [CrossRef]
12. Zhu, Y.; Wang, T.; Zhao, N. Arctic Puffin Optimization Algorithm Integrating Opposition-Based Learning and Differential Evolution with Engineering Applications. *Biomimetics* **2025**, *10*, 767. [CrossRef]
13. Ren, L.; Wang, D.; Yan, X.; Zhang, Y.; Wang, J. A Novel Chaotic Particle Swarm Optimized Backpropagation Neural Network PID Controller for Four-Switch Buck–Boost Converters. *Actuators* **2024**, *13*, 464. [CrossRef]

14. Dhanasekaran, B.; Jagatheesan, K.; Samanta, S.; Baskran, A.; Naidu, K. Multiobjective-Based Cuckoo Search Algorithm-Optimized PID Controller for Frequency Regulation of an Interconnected Power System. *J. Hum.-Cent. Des. Manuf.* **2025**, *1*, 25–45. [CrossRef]
15. Proaño, P.; Pozo, M.; Gallardo, C.; Camacho, O. Non-linear PID control of AC current and DC voltage for a photovoltaic system operating on a microgrid. *Results Control Optim.* **2025**, *18*, 100514. [CrossRef]
16. Parvizi, P.; Amidi, A.M.; Zangeneh, M.R.; Riba, J.-R.; Jalilian, M. A Taxonomy of Robust Control Techniques for Hybrid AC/DC Microgrids: A Review. *Eng* **2025**, *6*, 267. [CrossRef]
17. Nejlaoui, M.; Alghafis, A.; Alqahtani, N.A. Optimal Fractional Order PID Controller Design for Hydraulic Turbines Using a Multi-Objective Imperialist Competitive Algorithm. *Fractal Fract.* **2026**, *10*, 46. [CrossRef]
18. Camacho, O.; Vega, S.; Herrera, M.; Di Teodoro, A.; Gude, J.J. A fractional order PID-based sliding mode controller approach for chemical processes. *Results Control Optim.* **2025**, *20*, 100592. [CrossRef]
19. Zhmud, V.; Dimitrov, L. Control of Linear Multichannel Objects with Numerical Optimization. *Appl. Sci.* **2025**, *15*, 8927. [CrossRef]
20. Zambrano-Gutierrez, D.F.; Valencia-Rivera, G.H.; Avina-Cervantes, J.G.; Amaya, I.; Cruz-Duarte, J.M. Designing Heuristic-Based Tuners for Fractional-Order PID Controllers in Automatic Voltage Regulator Systems Using a Hyper-Heuristic Approach. *Fractal Fract.* **2024**, *8*, 223. [CrossRef]
21. Kumar, S.; Singh, H.P.; Ali, M.; Sait, A.R.W. Earthquake-Resilient Structural Control Using PSO-Based Fractional Order Controllers. *Fractal Fract.* **2025**, *9*, 759. [CrossRef]
22. Gupta, D.K.; Dei, G.; Soni, A.K.; Jha, A.V.; Appasani, B.; Bizon, N.; Srinivasulu, A.; Nsengiyumva, P. Fractional order PID controller for load frequency control in a deregulated hybrid power system using aquila optimization. *Results Eng.* **2024**, *23*, 102559. [CrossRef]
23. Tran, A.-T.; Duong, M.P.; Truong, P.; Shim, J.W.; Lim, C.P. An improved arctic puffin optimization-based multi-objective approach with novel cascade dual FOPID control for frequency regulation in standalone microgrids. *Energy Rep.* **2025**, *14*, 4976–4991. [CrossRef]
24. Liu, Y.; Tang, Y.; Hua, C. Multi-objective nutcracker optimization algorithm based on fast non-dominated sorting and elite strategy for grid-connected hybrid microgrid system scheduling. *Renew. Energy* **2025**, *242*, 122455. [CrossRef]
25. Almutairi, S.; Anayi, F.; Packianather, M.; Shouran, M. An Optimal Two-Stage Tuned PIDF + Fuzzy Controller for Enhanced LFC in Hybrid Power Systems. *Sustainability* **2025**, *17*, 9109. [CrossRef]
26. Samimi, A.; Nikzad, M.; Zakipour, A. Optimal sizing model of battery energy storage in a droop-controlled islanded multi-carrier microgrid based on an advanced frequency droop model. *Sci. Rep.* **2025**, *15*, 2540. [CrossRef]
27. Abumeteir, H.A.; Vural, A.M. Design and Optimization of Fractional Order PID Controller to Enhance Energy Storage System Contribution for Damping Low-Frequency Oscillation in Power Systems Integrated with High Penetration of Renewable Sources. *Sustainability* **2022**, *14*, 5095. [CrossRef]
28. Cao, J.-Y.; Liang, J.; Cao, B.-G. Optimization of fractional order PID controllers based on genetic algorithms. In *2005 International Conference on Machine Learning and Cybernetics, Guangzhou, China, 18–21 August 2005*; IEEE: New York, NY, USA, 2005; Volume 9, pp. 5686–5689. [CrossRef]
29. Khodadoost, S.; Saraee, M.; Talatahari, S.; Sareh, P. Optimal design of fractional-order proportional integral derivative controllers for structural vibration suppression. *Sci. Rep.* **2024**, *14*, 17207. [CrossRef]
30. Nejlaoui, M.; Najlawi, B.; Alsagri, A.S. A multi-objective methodology for multi-criteria engineering design. *Appl. Soft Comput.* **2020**, *91*, 106204. [CrossRef]
31. Najlaoui, B.; Alghafis, A.; Sadig, H.; Raouf, E.A.; Hassen, M.A. Multi-Objective Design Optimization and Experimental Investigation of a Low-Cost Solar Desalination System Under Al Qassim Climate. *Sustainability* **2025**, *17*, 1771. [CrossRef]
32. Agha Kassab, F.; Rodriguez, R.; Celik, B.; Locment, F.; Sechilariu, M. A Comprehensive Review of Sizing and Energy Management Strategies for Optimal Planning of Microgrids with PV and Other Renewable Integration. *Appl. Sci.* **2024**, *14*, 10479. [CrossRef]
33. Qu, Z.W.; Younis, W.; Liu, X.L.; Junejo, A.K.; Almutairi, S.Z.; Wang, P. Optimized PID controller for load frequency control in multi-source and dual-area power systems using PSO and GA algorithms. *IEEE Access* **2024**, *12*, 186658–186678. [CrossRef]
34. Datta, U.; Kalam, A.; Shi, J. Battery Energy Storage System for Aggregated Inertia-Droop Control and a Novel Frequency Dependent State-of-Charge Recovery. *Energies* **2020**, *13*, 2003. [CrossRef]
35. Mekhamer, A.S.; Hasanien, H.M.; Alharbi, M.; Tostado-Veliz, M.; Jurado, F.; Zaky, D.A. Coati optimization algorithm-based optimal frequency control of power systems including storage devices and electric vehicles. *J. Energy Storage* **2024**, *93*, 112196. [CrossRef]
36. Saadatmand, M.; Gharehpetian, G.B.; Kamwa, I.; Siano, P.; Guerrero, J.M.; Haes Alhelou, H. A Survey on FOPID Controllers for LFO Damping in Power Systems Using Synchronous Generators, FACTS Devices and Inverter-Based Power Plants. *Energies* **2021**, *14*, 5983. [CrossRef]

37. Najlaoui, B.; Alghafis, A.; Nejlaoui, M. Robust design of a low-cost flat plate collector under uncertain design parameters. *Energy Rep.* **2023**, *10*, 2950–2961. [CrossRef]
38. Nejlaoui, M.; Alghafis, A.; Sadig, H. Six sigma robust multi-objective design optimization of flat plate collector system under uncertain design parameters. *Energy* **2022**, *239*, 121883. [CrossRef]
39. Mohammed, R.; Shaik, A.S.; S, M.L.L.; B, S.R.S.V.; Mohammed, S.; Murthy, K.K. Mechanical performance and python-based TOPSIS ranking of carbon-filled Kevlar/Basalt/S-glass hybrid epoxy composites for automotive structural applications. *Sci. Rep.* **2026**, *16*, 12228. [CrossRef]

Disclaimer/Publisher's Note: The statements, opinions and data contained in all publications are solely those of the individual author(s) and contributor(s) and not of MDPI and/or the editor(s). MDPI and/or the editor(s) disclaim responsibility for any injury to people or property resulting from any ideas, methods, instructions or products referred to in the content.